mpi

INFORMATIK

An Empirical Model for
Heterogeneous Translucent
Objects

Christian Fuchs   Michael Goesele
Tongbo Chen   Hans-Peter Seidel

FORSCHUNGSBERICHT   RESEARCH REPORT

MAX-PLANCK-INSTITUT
FÜR
INFORMATIK

Authors' Addresses

Christian Fuchs
Max-Planck-Institut für Informatik
Stuhlsatzenhausweg 85
66123 Saarbrücken
cfuchs@mpi-sb.mpg.de

Michael Goesele
Max-Planck-Institut für Informatik
Stuhlsatzenhausweg 85
66123 Saarbrücken
goesele@mpi-sb.mpg.de

Tongbo Chen
Max-Planck-Institut für Informatik
Stuhlsatzenhausweg 85
66123 Saarbrücken
tongbo@mpi-sb.mpg.de

Hans-Peter Seidel
Max-Planck-Institut für Informatik
Stuhlsatzenhausweg 85
66123 Saarbrücken
hpseidel@mpi-sb.mpg.de

Abstract

We introduce an empirical model for multiple scattering in heterogeneous translucent objects for which classical approximations such as the dipole approximation to the diffusion equation are no longer valid. Motivated by the exponential fall-off of scattered intensity with distance, diffuse subsurface scattering is represented as a sum of exponentials per surface point plus a modulation texture. Modeling quality can be improved by using an anisotropic model where exponential parameters are determined per surface location and scattering direction. We validate the scattering model for a set of planar object samples which were recorded under controlled conditions and quantify the modeling error. Furthermore, several translucent objects with complex geometry are captured and compared to the real object under similar illumination conditions.

1 Introduction and Motivation

Translucency is an important effect in realistic image synthesis – many daily life objects such as skin, fruits, or wax are translucent. Although the perception of translucency is not yet fully understood [FJB04], it is clear that humans immediately notice when translucency is wrongly missing. While many recent publications deal with the rendering side of translucent objects (see, e.g., [JMLH01, CTW*04, GLL*04] for a comprehensive overview), only very few deal with the problem of creating digital models of real translucent objects with heterogeneous material properties as shown in Figure 1.

The light scattering behavior inside a translucent object can be captured by determining a detailed volumetric model of the object's internal structure. Given light transport parameters for each point on the object's surface and inside its volume and a sufficiently accurate (and complex) light transport simulation, perfect photorealistic renderings of the object under arbitrary lighting conditions can be created. Unfortunately, both model creation and evaluation are quite complex and resource-consuming. Chen et al. [CTW*04] propose therefore e.g. to measure scattering parameters for homogeneous materials as described in [JMLH01] and to determine their volumetric distribution using solid texture synthesis or classification methods for volume datasets. Alternatively, the object's complete light interaction properties can be recorded in the form of a general BSSRDF [NRH*77] or reflectance field [DHT*00]. By introducing the assumption that light transport is dominated by diffuse multiple scattering, the problem's dimensionality can be greatly reduced yielding a reasonable acquisition and storage effort [GLL*04].

Although its modeling capabilities are limited, many rendering systems use the dipole approximation to the diffusion equation [JMLH01] to model the multiple scattering contribution inside translucent objects. Light transport in strongly heterogeneous objects such as the example shown in Figure 1 can however not be modeled faithfully. Determining model parameters for locally non-flat objects by inverting the dipole approximation is furthermore not possible due to the underlying assumption of an infinite half-space of homogeneous material.

The goal of this paper is to introduce an empirical BSSRDF model which compactly describe the multiple scattering properties of inhomogeneous translucent objects based on real measured data. Global light transport due to multiple scattering inside the object is hereby modeled by a sum of exponential functions per surface point. Additional surface detail is included by a modulation texture. Anisotropic scattering behavior (e.g. caused by material with preferred scattering direction or heterogeneous material structure) can be modeled if exponential parameters are determined

per surface location and scattering direction. By moving from the physically motivated dipole model to a more general representation, we gain the required degrees of freedom to describe the inhomogeneities which can include a non-monotonic fall-off or rotationally asymmetric behavior. Still, the model is well enough adapted to the multiple scattering behavior to model its properties realistically.

The remainder of the paper is structured as follows: After reviewing previous work in Section 2 we describe the empirical model in detail (Section 3). We then validate our approach by acquiring subsurface scattering models for a set of planar material samples and analyzing the resulting errors and the modeling quality (Section 4). We show that heterogeneous objects can be described better by the proposed model than by a spatially varying dipole model. In Section 5, we furthermore create complete models for several complex objects to prove the applicability of the approach for objects with complex geometry for which measurement conditions are more difficult.

2   Previous Work

Compared to the number of publications dealing with various rendering aspects of translucent objects there are only a few papers about object modeling. Jensen et al. [JMLH01] introduced the dipole approximation to model the light transport in homogeneous translucent objects. They furthermore measured the required physical properties (scattering and absorption coefficients) for several materials and provided a heuristic to create synthetic inhomogeneous models. This process has been made more intuitive by a reparameterization of the scattering parameters in [JB02]. Shell texture functions
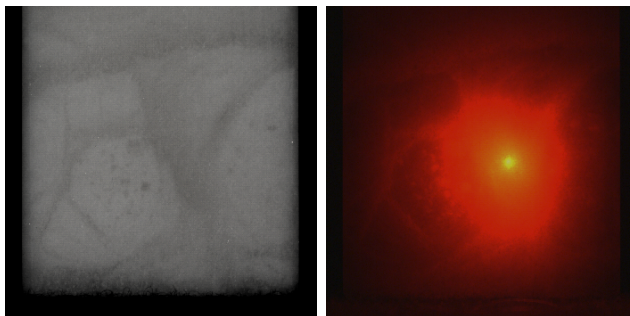

Figure 1: *Left:* Alabaster block with heterogeneous scattering properties under diffuse illumination (image contrast enhanced). *Right:* Resulting asymmetric highlight when a single point on the surface is illuminated.

(STF) [CTW*04] are a general texture function for complex objects intended as a fast rendering primitive. STFs can model translucency by combining a volumetric model of a thick material layer on an object's surface with a homogeneous object core. Scattering models for real heterogeneous objects can be acquired using standard volume modeling techniques which assign materials per voxel. Corresponding physical properties can then be looked up in published tables such as in [JMLH01].

The above techniques determine essentially the volumetric distribution of material properties. Creating exact models in this way is difficult as the volume is normally not directly accessible for measuring. Translucent objects can however also be modeled by database approach such as a reflectance field [DHT*00] which is closely related to the BSSRDF [NRH*77]. Due to their size and complexity these full 8D data structures are extremely cumbersome to acquire and handle in the general case. One approach to reduce complexity is to neglect the directional dependence of the data (treating the single scattering contribution as multiple scattering). This technique is used in the DISCO system [GLL*04] to acquire the 4D diffuse subsurface reflectance function as point-to-point transfer factors.

The goal of this paper is to combine the advantages of both approaches: Acquisition is performed similar to the DISCO approach which allows to efficiently capture a large amount of reflectance samples. These samples are then used to determine the parameters of an empirical reflection model to create a compact representation of the object and to easily interpolate missing values.

3 Subsurface Light Transport Model

Jensen et al. [JMLH01] proposed to approximate multiple scattering in inhomogeneous materials by a set of coefficients for the dipole model per incident light position and a global modulation texture. Our model for subsurface light transport is based on their ideas but introduces two modifications: Modeling light fall-off by a sum of exponential functions and introducing an anisotropic component to model material behavior that depends on the scattering direction at each surface location.

3.1 Sum of Exponentials

The behavior of multiple scattering is strongly dominated by the exponential fall-off of the intensity. We therefore replace the physically motivated dipole model by a *sum of exponential functions* per incident light position. This

empirical approach improves modeling capabilities for heterogeneous material and allows to adapt to a more general surface geometry The model for the diffuse subsurface reflectance R_d between the incoming and outgoing position $\vec{x}_i$ and $\vec{x}_o$, respectively, becomes then:

$$R_d(\vec{x}_i \rightarrow \vec{x}_o) = \sum_{k=1}^{n} c_k(\vec{x}_i) \cdot e^{d_k(\vec{x}_i)|\vec{x}_o - \vec{x}_i|}. \tag{1}$$

The multiple scattering behavior is determined for each surface position by the parameters $c_k(\vec{x}_i)$ and $d_k(\vec{x}_i)$. Note that these parameters have no physical interpretation. In our experience, $n = 3$ proved to be sufficient for most materials (see Section 5 for more details). For physically plausible behavior, we have to ensure convergence during the modeling process, i.e., $R_d(\vec{x}_i \rightarrow \vec{x}_o) \rightarrow 0$ for $|\vec{x}_i - \vec{x}_o| \rightarrow \infty$.

While the global light transport is modeled by the sum of exponentials, volumetric structures close to the surface at an outgoing position $\vec{x}_o$ are still modeled by a modulation texture $\alpha(\vec{x}_o)$, i.e., the overall diffuse scattering contribution S_d is

$$S_d(\vec{x}_i \rightarrow \vec{x}_o) = \alpha(\vec{x}_o)R_d(\vec{x}_i \rightarrow \vec{x}_o). \tag{2}$$

This provides a reasonable compromise between a full volumetric model that can also model parallax effects inside the material and modeling efficiency while still providing means to represent realistic surface structures.

3.2 Anisotropic Model

Like previous models, the above model assumes a rotationally symmetric behavior of the multiple scattering component. This is frequently inaccurate, e.g., for heterogeneous material (see Figure 1) or for material with a preferred scattering direction. We therefore introduce an *anisotropic model* by determining a set of parameters for the exponential model per direction between $\vec{x}_i$ and $\vec{x}_o$. For rendering, we blend between their contributions using a suitable weighting function $w_l(\vec{x}_i, \vec{x}_o)$ (e.g., a hat function for linear interpolation):

$$R_d(\vec{x}_i \rightarrow \vec{x}_o) = \sum_{l=1}^{m} w_l(\vec{x}_i, \vec{x}_o) \sum_{k=1}^{n} c_{kl}(\vec{x}_i) \cdot e^{d_{kl}(\vec{x}_i)|\vec{x}_o - \vec{x}_i|}. \tag{3}$$

4 Validation for Planar Surfaces

To validate our model for diffuse subsurface light transport against real data we first perform tests for planar surfaces. This removes many possible error
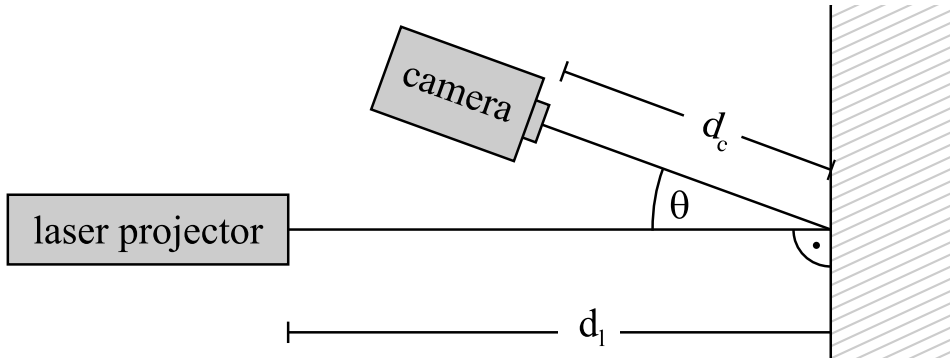
Figure 2: Planar acquisition setup. The laser beam hits the test surface almost perpendicularly from a distance d_l of about $850\,\text{mm}$. The camera observes the surface from the closest possible angle without obstructing the laser and a distance d_c of about $600\,\text{mm}$.

sources during acquisition and allows us to study the quality of the model for heterogeneous materials and simple geometry under ideal conditions. Measurements of real objects with complex geometry show the practical applications and limitations in Section 5.

4.1   Acquisition Setup

The acquisition setup for planar surfaces is shown in Figure 2. The focused beam of an Omicron-Laserage 3-color laser projector illuminates the surface perpendicularly. Images of a small measurement area (typically $20{\times}20\,\text{mm}$) are captured separately per color channel with a photometrically calibrated black-and white high-dynamic range video camera (SiliconVision Lars III). The narrow laser spot sweeps the surface densely and the spot location in captured images is determined with sub-pixel accuracy. For each pixel, we select the input image where the laser spot position $\vec{x}_i$ is best centered in the pixel's sampling area in order to achieve a near-regular sampling. All pixels with intensity values above a threshold defined by the camera noise floor are then directly used as samples $s(\vec{x}_i, \vec{x}_o)$ of the diffuse scattering contribution $S_d(\vec{x}_i \rightarrow \vec{x}_o)$ for further processing. Depending on the material, the dynamic range of used samples is on the order of 1:10,000.

4.2   Model Fitting

The acquisition process yields a dense sampling of R_d. Each pixel directly lit by the laser in one of the selected input images defines a location $\vec{x}_i$. All

other valid pixels in one of these images are samples of $R_d(\vec{x}_i \to \vec{x}_o)$. The parameters of the proposed model are computed in a two step process.

First, the parameters $c_{kl}(\vec{x}_i)$ and $d_{kl}(\vec{x}_i)$ of the diffuse reflectance function R_d are fitted for each selected input image (corresponding to the spot location $\vec{x}_i$) using standard Levenberg-Marquardt optimization. We use an objective function

$$O_l = \log \frac{\sum_{k=1}^{n} c_{kl}(\vec{x}_i) \cdot e^{d_{kl}(\vec{x}_i)|\vec{x}_o - \vec{x}_i|}}{s(\vec{x}_i, \vec{x}_o)} \tag{4}$$

with logarithmic error model. This leads to a uniform distribution of relative errors independent of the absolute intensity values and is therefore well adapted to the problem. In the anisotropic case, only those samples are included in the fitting that are associated with the direction under consideration.

Experiments with three channel RGB data have shown that in some cases fitting stability can be improved and modeling error decreased by determining only a single set of parameters $c_{kl}(\vec{x}_i)$ and $d_{kl}(\vec{x}_i)$ for the exponential fall-off. Color is thus modeled as a scale factor per channel avoiding (and suppressing) color shifts with distance. The model from Equation 3 becomes then

$$R_d(\vec{x}_i \to \vec{x}_o) = \begin{pmatrix} 1 \\ s_g(\vec{x}_i) \\ s_b(\vec{x}_i) \end{pmatrix} \sum_{l=1}^{m} w_l(\vec{x}_i, \vec{x}_o) \sum_{k=1}^{n} c_{kl}(\vec{x}_i) \cdot e^{d_{kl}(\vec{x}_i)|\vec{x}_o - \vec{x}_i|} \tag{5}$$

with scaling factors $s_g(\vec{x}_i)$ and $s_b(\vec{x}_i)$ for the green and blue color channel, respectively.

Once the parameters of the exponential model are known, the modulation texture $\alpha(\vec{x}_o)$ can be determined as average multiplicative correction factor

$$\alpha(\vec{x}_o) = \frac{1}{|\mathcal{X}|} \sum_{\mathcal{X}} \frac{s(\vec{x}_i, \vec{x}_o)}{R_d(\vec{x}_i \to \vec{x}_o)} \tag{6}$$

using all samples $\mathcal{X}$ within a medium intensity range, i.e., $\mathcal{X} := \{\vec{x}_o \mid t_1 > s(\vec{x}_i, \vec{x}_o) > t_2\}$ with thresholds t_1 and t_2. The scattering behavior of these samples is dominated by multiple scattering and camera noise is still at a minimum.

4.3 Results

Figure 3 shows the reflectance samples collected for a single image and a single color channel of the marble example (Figure 5). Both the dipole model and the proposed exponential model were fitted to the captured data. The
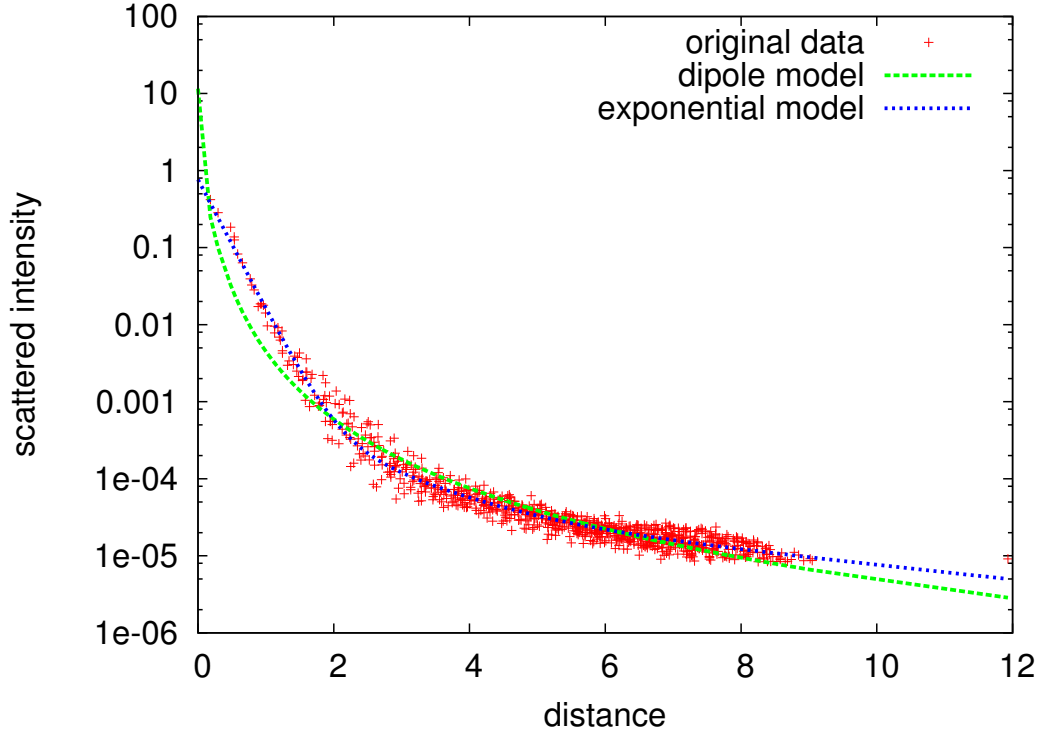
Figure 3: Comparison between dipole model and exponential model. The data corresponds to a single lit surface point in the marble example (Figure 5).

comparison does not include the modulation texture $\alpha(\vec{x}_o)$. It can be clearly seen that the sum of exponentials approximates the data much better than the dipole model. Furthermore, the error of the dipole model correlates strongly with the marble structure seen on the left whereas it is more uniformly distributed for the exponential model.

Figure 4 *left* shows an example image for a piece of inhomogeneous marble illuminated by a laser spot and the corresponding reconstruction using the isotropic model with modulation texture. The reconstruction error

$$E(\vec{x}_i \rightarrow \vec{x}_o) = \frac{\alpha(\vec{x}_o)R_d(\vec{x}_i \rightarrow \vec{x}_o)}{s(\vec{x}_i, \vec{x}_o)} \tag{7}$$

for this image is shown on the right for the case of an isotropic and a 4 and 8 segment anisotropic model, respectively. The error clearly decreases for the anisotropic case. This is also evident in Figure 5 *right* where the

7

material	isotropic model	anisotropic model (8 segments)
marble	0.0397	0.0175
apple	0.0045	0.0020
sponge	0.0411	0.0307
candle (chunky)	—	0.0082
grey marble (polished)	—	0.0590
grey marble (diffuse)	—	0.0288
material	*isotropic model*	*anisotropic model (8 segments)*
marble	*0.0336*	*0.0189*
apple	—	—
sponge	—	—
candle (chunky)	*0.0225*	*0.0162*
grey marble (polished)	*0.2354*	*0.1680*
grey marble (diffuse)	*0.0691*	*0.0566*

Table 1: Mean of reconstruction error $E(\vec{x}_i)$ for various planar samples (green channel). The upper pair of values show the error when fitting the full exponential model per color channel (Equation 3). The lower pair of values (in italics) show the error when fitting a single exponential fall-off (Equation 5).

reconstruction error $E(\vec{x}_i)$ defined as

$$\log E(\vec{x}_i) = \sqrt{\frac{1}{|\mathcal{X}|} \cdot \sum_{\mathcal{X}} (\log E(\vec{x}_i \to \vec{x}_o))^2} \tag{8}$$

with $\mathcal{X} := \{\vec{x}_o \mid s(\vec{x}_i, \vec{x}_o) > t\}$ and a threshold t is plotted for all image locations l. Table 1 gives the mean of the error $E(\vec{x}_i)$ for various materials and the two versions of the exponential model. It is evident that the more general model shown in Equation 3 yields only in some cases a smaller overall error than the model with a single exponential fall-off and scaling factors for the individual channels (Equation 5). The anisotropic version yields however in both cases a lower mean reconstruction error.

5 Modeling Arbitrary Surfaces

To acquire data from objects with complex geometry, we built an acquisition setup similar to the one used for the DISCO system [GLL*04]: The

object is placed on a turntable, point-wise illuminated by a laser projector and captured with the HDR video camera from various positions. Data is then collected from all images in which a particular location on the object was illuminated yielding an incident light position $\vec{x}_i$ and a set of reflectance samples $s(\vec{x}_i, \vec{x}_o)$ located on the object surface. The object geometry is modeled as a triangular mesh. Similar to the planar case, we select for each vertex in the mesh the closest light position $\vec{x}_i$ and derive per-vertex parameters for the exponential model from this set of samples.

Compared to the planar case, model fitting becomes much more difficult due to several reasons: First, geometry and surface effects such as first surface reflection and interreflections become important and change the total scattering behavior. For thin geometric structures and optically thin material, single scattering can be observed. Depending on the configuration during acquisition, data is only sparsely available and sampled irregularly. Finally, uncertainty in the observed data increases drastically due to inaccuracy in the geometry model, misregistration between input images and geometry and other measurement error. Fitting of the anisotropic model as described in Equation 5 proved to be too unstable. We therefore resorted to the isotropic model with a single exponential fall-off for all three color channels

$$\widetilde{R_d}(\vec{x}_i \rightarrow \vec{x}_o) = \alpha(\vec{x}_o) \cdot \begin{pmatrix} 1 \\ s_g(\vec{x}_i) \\ s_b(\vec{x}_i) \end{pmatrix} \cdot \sum_{k=1}^{n} c_k(\vec{x}_i) \cdot e^{d_k(\vec{x}_i)|\vec{x}_o - \vec{x}_i|}. \qquad (9)$$

All parameters (s_g, s_b, c_k, d_k) are determined per-vertex with $n = 3$ using Levenberg-Marquardt optimization. The modulation texture $\alpha(\vec{x}_o)$ is determined as higher resolution texture. In cases where fitting still was unstable (mainly due to incorrect detection of the highlight position on the geometry), the number of exponents n was reduced, vertices for which no stable fit could be achieved were were filtered out and interpolated from neighboring vertices.

5.1   Results

Fig. 6 compares photon map renderings [Jen01] of a captured model to real images of an alabaster pig under similar lighting conditions. In the top example, a point light source was placed directly behind the object so that only scattered light is visible. The second example is illuminated from the right; parts of the model are in direct illumination.

The exponential model represents many of the scattering effects such as the dark leg in the top example quite well. Most of the local surface detail is

9

preserved by the modulation texture. The body of the pig appears however too bright and regions close to incident illumination are often underestimated. This is caused by several effects including first surface reflection and single scattering, uncertainty in the modeling and rendering artifacts – effects that are mostly avoided in the planar example. These artifacts are also much less visible in typical scenes with partially front-lit objects (see Fig. 6 (bottom) and the accompanying video).

Figure 7 shows the candle model next to a photograph of the real candle under similar illumination. Again, the intensity far away from incident light positions is overestimated. First surface reflection of the quite specular is suppressed in the photograph by a pair of polarizing filters to make the images comparable.

6   Conclusion and Future Work

We presented a new empirical model for translucent objects that models diffuse multiple scattering as a sum of exponential functions. We first showed the validity of the model for planar geometry and compared it to the dipole model. The planar examples demonstrate also that the anisotropic version improves the quality of the resulting models and is therefore preferable.

Complexity increases when the model is applied to objects with complex geometry. This is mainly due to new sources of uncertainty in the measurement process and not due to fundamental limitations of the proposed model. Nevertheless, the resulting models look convincing despite the remaining artifacts. These become even less visible if the models are illuminated with more common "soft lighting" instead of hard point light source illumination.

Overall, the proposed model provides a good approximation to the multiple scattering behavior of heterogeneous translucent objects. Final models are small (typically on the order of $5\,\mathrm{MB}$) and well suited for fast rendering. While the final goal to efficiently acquire and handle translucent objects has certainly not yet been reached, we believe that the presented work serves as an important step in this direction.

An open problem for the future is acquiring the single scattering contribution for inhomogeneous translucent objects. This would strongly enlarge the class of possible materials but it also strongly increases complexity due to the directional variation of single scattering. A further direction for future work is certainly the simplification and acceleration of the acquisition process in order to make the technique applicable for a broader audience.

References

[CTW*04] CHEN Y., TONG X., WANG J., LIN S., GUO B., SHUM H.-Y.: Shell Texture Functions. *ACM Trans. Graph. (SIGGRAPH 2004) 23*, 3 (2004), 343–353.

[DHT*00] DEBEVEC P., HAWKINS T., TCHOU C., DUIKER H.-P., SAROKIN W., SAGAR M.: Acquiring the Reflectance Field of a Human Face. In *SIGGRAPH 2000* (2000), pp. 145–156.

[FJB04] FLEMING R. W., JENSEN H. W., BÜLTHOFF H. H.: Perceiving Translucent Materials. In *APGV '04: 1st Symp. on Applied Perception in Graphics and Visualization* (2004), pp. 127–134.

[GLL*04] GOESELE M., LENSCH H. P. A., LANG J., FUCHS C., SEIDEL H.-P.: DISCO – Acquisition of Translucent Objects. *ACM Trans. Graph. (SIGGRAPH 2004) 23*, 3 (2004), 835–844.

[JB02] JENSEN H. W., BUHLER J.: A Rapid Hierarchical Rendering Technique for Translucent Materials. In *SIGGRAPH 2002* (2002), pp. 576–581.

[Jen01] JENSEN H. W.: *Realistic Image Synthesis Using Photon Mapping.* A. K. Peters, 2001.

[JMLH01] JENSEN H. W., MARSCHNER S. R., LEVOY M., HANRAHAN P.: A Practical Model for Subsurface Light Transport. In *SIGGRAPH 2001* (2001), pp. 511–518.

[NRH*77] NICODEMUS F. E., RICHMOND J. C., HSIA J. J., GINSBERG I. W., LIMPERIS T.: Geometrical Considerations and Nomenclature for Reflectance. NBS, 1977.
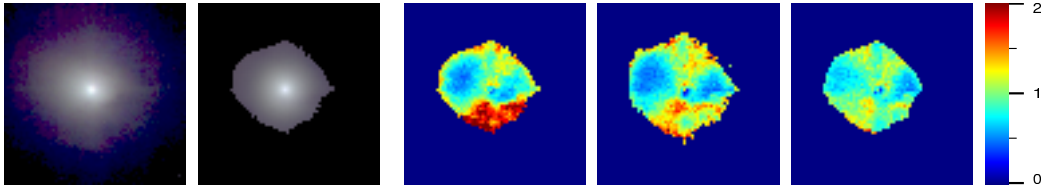
Figure 4: The marble example. *Left:* Input image and corresponding reconstruction (isotropic model with modulation texture, logarithmically scaled intensities). *Right:* Corresponding reconstruction error $E(\vec{x}_i \rightarrow \vec{x}_o)$ in the green channel for the isotropic model and the anisotropic model with 4 and 8 segments.
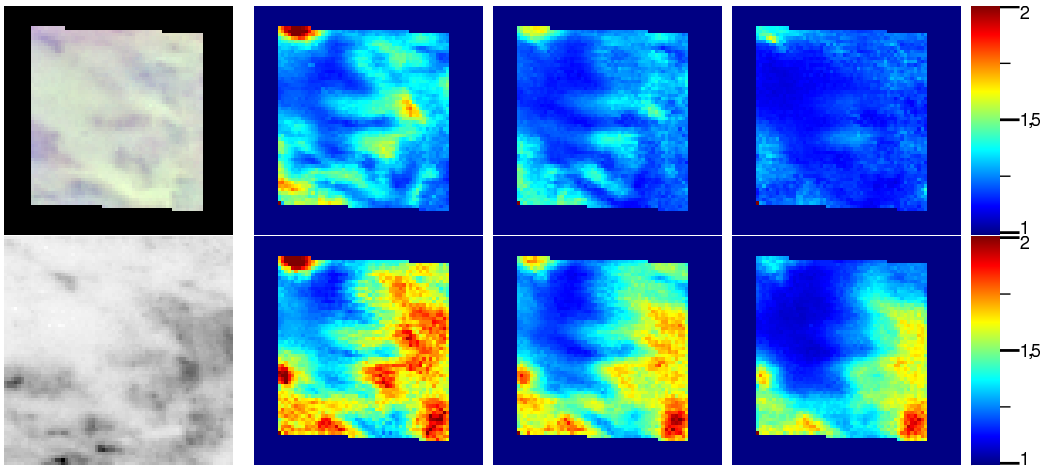

Figure 5: The marble example (contd., images show same surface area as in Figure 4). *Left:* Modulation texture and diffusely lit surface (black and white due to the camera used). *Right top:* Error $E(\vec{x}_i)$ for the model from Equation 5 in the green channel (isotropic model and anisotropic model with 4 and 8 segments). Note that $E(\vec{x}_i) = 1$ means perfect reconstruction. *Right bottom:* Error $E(\vec{x}_i)$ for the dipole model in the green channel (isotropic model and anisotropic model with 4 and 8 segments).
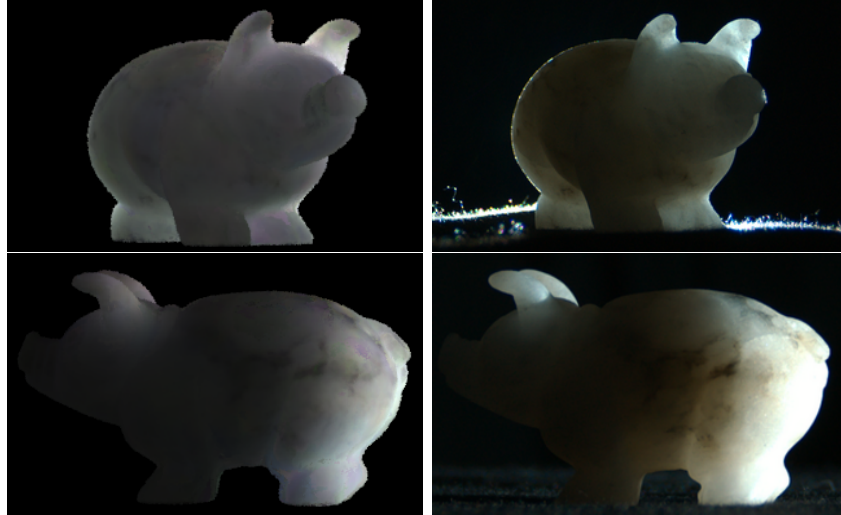
Figure 6: Comparison between renderings of our model (left) and photographs of the alabaster pig under similar lighting conditions. *Top:* Model illuminated by a point light source from behind. *Bottom:* Model illuminated from the right.
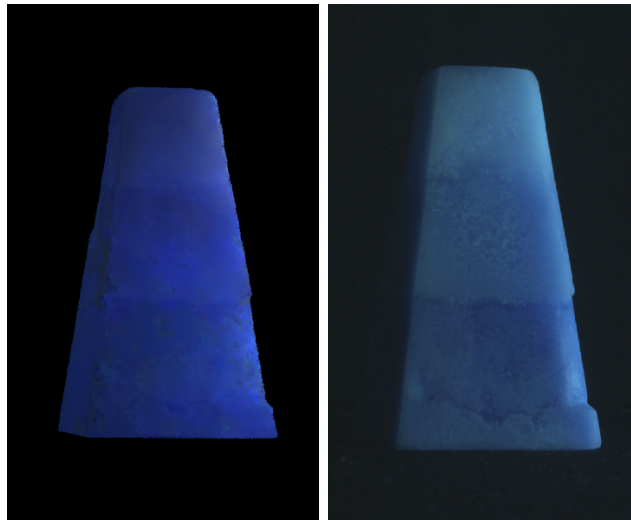

Figure 7: Comparison between rendered candle model and photograph both illuminated from the right. A pair of polarizing filters was used to suppress the specular reflection off the candle.

Below you find a list of the most recent technical reports of the Max-Planck-Institut für Informatik. They are available by anonymous ftp from `ftp.mpi-sb.mpg.de` under the directory `pub/papers/reports`. Most of the reports are also accessible via WWW using the URL `http://www.mpi-sb.mpg.de`. If you have any questions concerning ftp or WWW access, please contact `reports@mpi-sb.mpg.de`. Paper copies (which are not necessarily free of charge) can be ordered either by regular mail or by e-mail at the address below.

MPI-I-2005-4-006	C. Fuchs, M. Goesele, T. Chen, H. Seidel	An Emperical Model for Heterogeneous Translucent Objects
MPI-I-2005-4-005	G. Krawczyk, M. Goesele, H. Seidel	Photometric Calibration of High Dynamic Range Cameras
MPI-I-2005-4-004	C. Theobalt, N. Ahmed, E. De Aguiar, G. Ziegler, H. Lensch, M.A.,. Magnor, H. Seidel	Joint Motion and Reflectance Capture for Creating Relightable 3D Videos
MPI-I-2005-4-003	T. Langer, A.G. Belyaev, H. Seidel	Analysis and Design of Discrete Normals and Curvatures
MPI-I-2005-4-002	O. Schall, A. Belyaev, H. Seidel	Sparse Meshing of Uncertain and Noisy Surface Scattered Data
MPI-I-2005-4-001	M. Fuchs, V. Blanz, H. Lensch, H. Seidel	Reflectance from Images: A Model-Based Approach for Human Faces
MPI-I-2005-2-001	J. Hoffmann, Carla Gomes	Bottleneck Behavior in CNF Formulas
MPI-I-2005-1-007	I. Katriel, M. Kutz	A Faster Algorithm for Computing a Longest Common Increasing Subsequence
MPI-I-2005-1-002	I. Katriel, M. Kutz, M. Skutella	Reachability Substitutes for Planar Digraphs
MPI-I-2005-1-001	D. Michail	Rank-Maximal through Maximum Weight Matchings
MPI-I-2004-NWG3-001	M. Magnor	Axisymmetric Reconstruction and 3D Visualization of Bipolar Planetary Nebulae
MPI-I-2004-NWG1-001	B. Blanchet	Automatic Proof of Strong Secrecy for Security Protocols
MPI-I-2004-5-001	S. Siersdorfer, S. Sizov, G. Weikum	Goal-oriented Methods and Meta Methods for Document Classification and their Parameter Tuning
MPI-I-2004-4-006	K. Dmitriev, V. Havran, H. Seidel	Faster Ray Tracing with SIMD Shaft Culling
MPI-I-2004-4-005	I.P. Ivrissimtzis, W.-. Jeong, S. Lee, Y.a. Lee, H.-. Seidel	Neural Meshes: Surface Reconstruction with a Learning Algorithm
MPI-I-2004-4-004	R. Zayer, C. Rössl, H. Seidel	r-Adaptive Parameterization of Surfaces
MPI-I-2004-4-003	Y. Ohtake, A. Belyaev, H. Seidel	3D Scattered Data Interpolation and Approximation with Multilevel Compactly Supported RBFs
MPI-I-2004-4-002	Y. Ohtake, A. Belyaev, H. Seidel	Quadric-Based Mesh Reconstruction from Scattered Data
MPI-I-2004-4-001	J. Haber, C. Schmitt, M. Koster, H. Seidel	Modeling Hair using a Wisp Hair Model
MPI-I-2004-2-007	S. Wagner	Summaries for While Programs with Recursion
MPI-I-2004-2-002	P. Maier	Intuitionistic LTL and a New Characterization of Safety and Liveness

MPI-I-2004-2-001	H. de Nivelle, Y. Kazakov	Resolution Decision Procedures for the Guarded Fragment with Transitive Guards
MPI-I-2004-1-006	L.S. Chandran, N. Sivadasan	On the Hadwiger's Conjecture for Graph Products
MPI-I-2004-1-005	S. Schmitt, L. Fousse	A comparison of polynomial evaluation schemes
MPI-I-2004-1-004	N. Sivadasan, P. Sanders, M. Skutella	Online Scheduling with Bounded Migration
MPI-I-2004-1-003	I. Katriel	On Algorithms for Online Topological Ordering and Sorting
MPI-I-2004-1-002	P. Sanders, S. Pettie	A Simpler Linear Time 2/3 - epsilon Approximation for Maximum Weight Matching
MPI-I-2004-1-001	N. Beldiceanu, I. Katriel, S. Thiel	Filtering algorithms for the Same and UsedBy constraints
MPI-I-2003-NWG2-002	F. Eisenbrand	Fast integer programming in fixed dimension
MPI-I-2003-NWG2-001	L.S. Chandran, C.R. Subramanian	Girth and Treewidth
MPI-I-2003-4-009	N. Zakaria	FaceSketch: An Interface for Sketching and Coloring Cartoon Faces
MPI-I-2003-4-008	C. Roessl, I. Ivrissimtzis, H. Seidel	Tree-based triangle mesh connectivity encoding
MPI-I-2003-4-007	I. Ivrissimtzis, W. Jeong, H. Seidel	Neural Meshes: Statistical Learning Methods in Surface Reconstruction
MPI-I-2003-4-006	C. Roessl, F. Zeilfelder, G. Nürnberger, H. Seidel	Visualization of Volume Data with Quadratic Super Splines
MPI-I-2003-4-005	T. Hangelbroek, G. Nürnberger, C. Roessl, H.S. Seidel, F. Zeilfelder	The Dimension of C^1 Splines of Arbitrary Degree on a Tetrahedral Partition
MPI-I-2003-4-004	P. Bekaert, P. Slusallek, R. Cools, V. Havran, H. Seidel	A custom designed density estimation method for light transport
MPI-I-2003-4-003	R. Zayer, C. Roessl, H. Seidel	Convex Boundary Angle Based Flattening
MPI-I-2003-4-002	C. Theobalt, M. Li, M. Magnor, H. Seidel	A Flexible and Versatile Studio for Synchronized Multi-view Video Recording
MPI-I-2003-4-001	M. Tarini, H.P.A. Lensch, M. Goesele, H. Seidel	3D Acquisition of Mirroring Objects
MPI-I-2003-2-004	A. Podelski, A. Rybalchenko	Software Model Checking of Liveness Properties via Transition Invariants
MPI-I-2003-2-003	Y. Kazakov, H. de Nivelle	Subsumption of concepts in DL $\mathcal{FL}_0$ for (cyclic) terminologies with respect to descriptive semantics is PSPACE-complete
MPI-I-2003-2-002	M. Jaeger	A Representation Theorem and Applications to Measure Selection and Noninformative Priors
MPI-I-2003-2-001	P. Maier	Compositional Circular Assume-Guarantee Rules Cannot Be Sound And Complete
MPI-I-2003-1-018	G. Schaefer	A Note on the Smoothed Complexity of the Single-Source Shortest Path Problem
MPI-I-2003-1-017	G. Schäfer, S. Leonardi	Cross-Monotonic Cost Sharing Methods for Connected Facility Location Games
MPI-I-2003-1-016	G. Schäfer, N. Sivadasan	Topology Matters: Smoothed Competitive Analysis of Metrical Task Systems
MPI-I-2003-1-015	A. Kovács	Sum-Multicoloring on Paths
MPI-I-2003-1-014	G. Schäfer, L. Becchetti, S. Leonardi, A. Marchetti-Spaccamela, T. Vredeveld	Average Case and Smoothed Competitive Analysis of the Multi-Level Feedback Algorithm
MPI-I-2003-1-013	I. Katriel, S. Thiel	Fast Bound Consistency for the Global Cardinality Constraint
MPI-I-2003-1-012		- not published -
MPI-I-2003-1-011	P. Krysta, A. Czumaj, B. Voecking	Selfish Traffic Allocation for Server Farms
MPI-I-2003-1-010	H. Tamaki	A linear time heuristic for the branch-decomposition of planar graphs

| MPI-I-2003-1-009 | B. Csaba | On the Bollobás – Eldridge conjecture for bipartite graphs |
| MPI-I-2003-1-008 | P. Sanders | Polynomial Time Algorithms for Network Information Flow |